2000

Numerical Investigation of Passive and Active Control of Unsteady Compressible Flow

J.A.Ekaterinaris

J.A. Ekaterinaris and M.S. Chandrasekhara, "Numerical Investigation of Passive and Active Control of Unsteady Compressible Flow", AIAA Paper 00-4417, Denver, CO, Aug. 2000.

A00-39903

AIAA-2000-4417

Numerical Investigation of Passive and Active Controls of Unsteady Compressible Flow

J. A. Ekaterinaris*
Nielsen Eng. & Research Inc.
Mountain View, CA 94043-2212

and

M. S. Chandrasekhara†
Naval Postgraduate School
Monterey, California

Abstract

Numerical simulations of flow controls applied to airfoils undergoing oscillatory motion in compressible flow are presented. Currently available efficient and accurate numerical methods for the full compressible flow equations and advanced turbulence models are used for the numerical predictions. Time-accurate computations at low angles of incidence indicate development of flow unsteadiness for the slatted airfoil. It is found, however, that the leading-edge slat effectively suppresses dynamic stall, it improves dynamic blade response, and reduces flow separation, for compressible flow speeds. It was also found that dynamic stall can be suppressed using control with pulsating jets.

1 Introduction

The main obstacles that need to be surpassed in order to achieve significant improvements in aerodynamic performance of helicopter rotors and obtain increases of the maximum thrust are the reduction or elimination of dynamic stall and improvement of the airfoil lift capacity. Improvements in airfoil lift capacity without significant compromises in pitching moment or drag penalties is unrealistic for conventional airfoils. Lift augmentation by increases of blade area of single-element rotors will increase the blade weight and may result in a decrease of useful payload. On the other hand, increasing the lift by adding camber to the airfoil results in high pitching moment level which is undesirable because it leads to higher control loading. In addition, cambered airfoils have poor dynamic stall characteristics that lead to structural vibration. Therefore, development of active and passive flow controls for airfoils undergoing dynamic motion, which can offer the desired improvements, has been the subject of experimental and theoretical investigation for the past decades (see Ref. [12], [2], [3], [10], and [11]).

Dynamic stall is a limiting factor for more widespread use of helicopters in both military and civilian applications. It reduces the maximum cruise speed of helicopters because it generates excessive loads on the rotor and the flight controls. Dynamic stall is characterized by a strong vortex, referred to as the dynamic stall vortex, which usually originates at the leading edge during the pitch-up motion of the retreating blade. This vortex grows and, as it convects towards the trailing edge, causes abrupt variations in lift, a sharp increase in drag, and a large undesirable nose-down pitching moment. Because of the negative impact of dynamic stall, basic research (see Ref. [7] and references therein) has focused on understanding how to control and possibly eliminate its occurrence. Passive and active flow controls can be used to reduce or possibly completely eliminate dynamic stall on helicopter rotor blades.

Since much of the dynamic stall flow is vorticity dominated, effective flow control requires management of the unsteadiness produced at the leading edge. Thus, alterations of the flow at the leading-edge region are most effective in controlling dynamic stall. It was

---

* Senior Research Scientist, Associate Fellow, AIAA.
† Research Prof. and Associate Dir. Navy-NASA Joint Institute of Aeronautics, Associate Fellow, AIAA.

shown in experiments that for thin airfoils, which are common in helicopter rotor applications, alterations of the flow at the leading–edge region were proven most effective in controlling dynamic stall [10], [2], [3] [12]. Therefore, several leading edge boundary layer control methods have been employed in rotorcraft applications. These methods include: steady blowing or suction [19], pulsating blowing, [10], [11], and [16] and boundary layer transition [2]. Another category of flow control methods which have been investigated are based on modifying the blade geometry. Examples include: passive controls, such as leading–edge slats [3], active airfoil geometry modifications, and other dynamic geometry controls such as nose drooping and dynamically deforming leading–edge geometry. Some of these methods have proven highly effective. It has been shown, for example, that oscillatory blowing is more effective than steady blowing in delaying dynamic stall [10], [11].

Leading–edge slats belong to the class of passive flow controls. The dynamic stall characteristics of a slatted airfoil was studied experimentally in Ref. [12]. It was shown [12], that use of slats reduces the hysteresis effects and increases the lift during the oscillation cycle. In addition, it was found that there are no adverse effects on drag and pitching moment characteristics. Passive flow controls are simple to implement and can considerably improve airfoil performance under both steady and unsteady flow conditions. Recent numerical investigations also concluded that simple passive flow control with leading edge slats [1] or dual element airfoils [18] of helicopter rotor blade flowfields can offer significant improvements to helicopter performance and alleviate detrimental effects of dynamic stall. The primary benefit of the leading–edge slat on a rotor blade is to improve the aerodynamic performance of the rotor in hover and forward flight. The maximum thrust generated by the rotor in hover is limited by blade stall. It was found that leading edge–slats [12] delay stall and increase the maximum thrust generated by the rotor. As a result, increases in useful payload can be realized because the leading–edge slat does not add a significant amount of weight.

Passive flow control obtained by a leading edge slat is investigated numerically for high Reynolds number, $Re_c = 5.0 \times 10^6$, compressible flow ($M_\infty = 0.4$). The effectiveness of this flow control in eliminating or delaying dynamic stall occurring under realistic helicopter flight conditions is considered. Particular emphasis is paid in revealing the structure of the unsteady flowfield and the mechanisms that cause delay of dynamic stall. This task is accomplished by performing numerical simulations and experiments. The generated data base of simulated flow controls supplements experimental findings, helps to better understand the mechanisms that contribute to control stall, and allows to determine the parameter range for optimal flow control.

The computational tool which is used in the present work has been extensively validated for unsteady flow computations and dynamic stall [4], [5], [6], and [8] by comparison with experimental data. Additional validation is performed using available measurements for a slatted airfoil to further increase the level of confidence of the numerical procedure and demonstrate its ability to accurately simulate the complex flow generated by the leading edge slat both over stationary and oscillating airfoils. Results are obtained first for compressible flow at fixed angles of incidence over the RC(6) – 08/106, 6° slat and the RC(6) – 08/210, 10° slat airfoils. Next computations for the oscillatory motion the baseline, RC(6) – 08, airfoil are obtained. Comparisons of the load hysteresis loops of the baseline airfoil, with the RC(6) – 08/106, 6° slat airfoil, and the RC(6) – 08/210, 10° slat airfoil are presented to demonstrate the the effectiveness of the leading edge slat in controlling dynamic stall.

Experimental [11] and numerical [9] investigations have demonstrated that pneumatic flow control with pulsating jet is effective in controlling dynamic stall. Therefore, flow control with pulsating jets over the baseline RC(6)–08 airfoil was attempted. It is found, however, that for high oscillation amplitudes and flows with significant compressibility effects, which cause shock formation at the leading edge region, pulsating flow control is not capable of controlling dynamic stall and flow separation. It is shown that application of flow control with pulsating jet for dynamic stall at smaller oscillation amplitudes and flows with milder compressibility effects is quite effective.

2 Numerical Implementation

Numerical simulation of complex flows over slatted airfoils require numerical solutions of the compressible Navier–Stokes equations. The governing equation are summarized in the next section. Compressibility effects are important for the Mach numbers of interest in the present investigation and use of numerical schemes with good shock capturing capabilities are needed. In addition, time–accurate computation of time–depended flows requires stable time integration methods which allow large time steps. An alternating direction implicit (ADI) numerical scheme which fulfills these requirements is also described.

2.1 Governing Equations

In the compressible flow simulations the thin–layer approximation of the Navier–Stokes equations is used. These equations in curvilinear, body–fitted coordinates (ξ, η) are.

$$\frac{\partial \mathbf{Q}}{\partial t} + \frac{\partial \mathbf{F}(\mathbf{q})}{\partial \xi} + \frac{\partial \mathbf{G}(\mathbf{q})}{\partial \eta} = \frac{\partial \mathbf{G}_v(\mathbf{q})}{\partial \eta} \qquad (1)$$

where $\mathbf{Q} = J^{-1}[\rho, \rho u, \rho v, e]^T = \mathbf{q}/J$ is the solution vector, J is the Jacobian of the coordinate transformation, and $\mathbf{F}$ and $\mathbf{G}$ are the flux vectors in curvilinear coordinates. For example, $\mathbf{F} = J^{-1}[\rho U,\ \rho u U + \xi_x p,\ \rho v U + \xi_y p,\ (e+p)U - \xi_t p]^T$, where U is the contravariant velocity component $U = \xi_x u + \xi_y v + \xi_t$, and u, v are the Cartesian velocity components. The pressure, p, for a calorically perfect gas, is related to the other variables through the equation of state as $p = (\gamma - 1)\left[e - 0.5\rho(u^2 + v^2)\right]$.

2.2 The Numerical Scheme

Space discretization of the convective fluxes is performed using upwinding and Roe's approximate Riemann solver [15]. Third order accurate, upwind biased formulas are used to evaluate the convective flux derivatives. The viscous terms are computed using second–order accurate central differences. The eddy viscosity is computed using the one–equation turbulence model of Spalart and Allmaras [17]. Essential details of the numerical algorithms are given next.

In the past years, several numerical investigations of dynamic stall of simple airfoils [4] and blades [5] have been performed with the code we use to simulate compressible flows. The computed results for dynamic stall cases were in agreement with measurements and they are summarized in the review of Ref. 6. The computer code solves the time dependent compressible flow equations in curvilinear body fitted coordinates. It has been developed for the numerical investigation of dynamic stall flows [4], [5] and has been also tested for other unsteady aerodynamic applications [6], [8]. It performs implicit time marching using the following alternating direction implicit (ADI) scheme.

$$\begin{aligned}
&\left[I + h_\xi\left(\nabla_\xi^b \widehat{A^+}_{i,j} + \Delta_\xi^f \widehat{A^-}_{i,j}\right)\right]^p \\
&\times \left[I + h_\eta\left(\nabla_\eta^b \widehat{B^+}_{i,j} + \Delta_\eta^f \widehat{B^-}_{i,j}\right.\right. \\
&\left.\left. - Re^{-1}\delta_\eta \widehat{M_{i,j}}\right)\right]^p \times \left(\tilde{Q}_{i,j}^{p+1} - \tilde{Q}_{i,j}^{p}\right) \\
&= -\left[\left(\tilde{Q}_{i,j}^{p} - Q_{i,j}^{n}\right) + h_\xi\left(\hat{F}_{i+1/2,j}^{p} - \hat{F}_{i-1/2,j}^{p}\right)\right. \\
&+ h_\eta\left(\hat{G}_{i,j+1/2}^{p} - \hat{G}_{i,j-1/2}^{p}\right) \\
&\left. - Re^{-1} h_\eta\left(\hat{S}_{i,j+1/2}^{p} - \hat{S}_{i,j-1/2}^{p}\right)\right] \qquad (2)
\end{aligned}$$

In this equation, $h_\xi = \Delta\tau/\Delta\xi$, etc., $\tilde{A}^\pm = (\partial\tilde{F}/\partial\tilde{Q})$, etc., are the flux Jacobian matrices, and Δ, ∇, and δ are the forward, backward and central difference operators, respectively. The quantities $\widehat{A^\pm_{i,j}}, \widehat{B^\pm_{i,j}}$ are Jacobian matrices from the linearization of the right hand side, and $\hat{F}_{i+1/2,j}$, $\hat{G}_{i,j+1/2}$, and $\hat{S}_{i,j+1/2}$ are numerical fluxes. Third-order accurate, upwind–biased formulas are used for the computation of the right hand side numerical fluxes $\hat{F}_{i,k+1/2}$, and $\hat{G}_{i,k+1/2}$. An one–equation turbulence models [17] is used for computations of high Reynolds number fully turbulent flows.

3 Results

Numerical solutions at various fixed angles of incidence $\alpha = 0^o, 5^o, 10^o, 15^o$ and 20^o were computed for the baseline RC(6) – 08, airfoil the, RC(6) – 08/106, 6^o slat airfoil, and the RC(6) – 08/210, 10^o slat airfoil at free stream speed $M_\infty = 0.4$, and fully turbulent flow at $Re_c = 5 \times 10^6$. Computations of the flow over the slatted airfoils are obtained on a single–block grid. The 315×121 point grid used for numerical solutions over the RC(6) – 08/106, is shown in Fig. 1. A similar 329×121 point grid is used for the numerical solutions over the RC(6) – 08/210, 10^o slat airfoil.

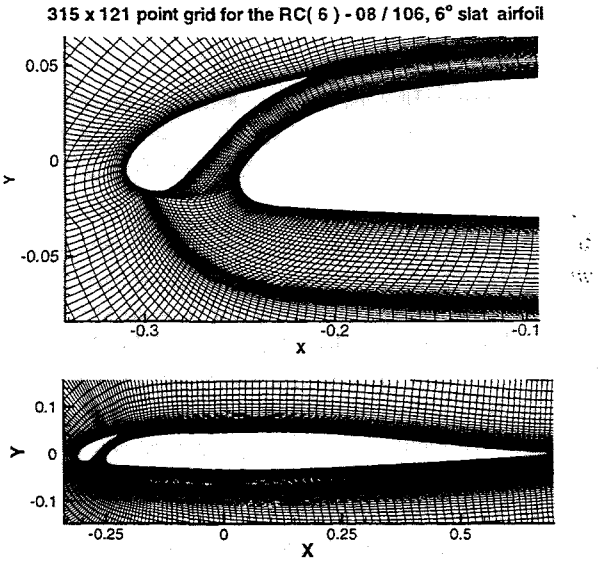

Fig. 1 Grid for the numerical simulation of the oscillating slatted airfoil.

3.1 Fixed Angles of Incidence

A steady–state fully turbulent flow solution was obtained for the 6^o slat airfoil at $M_\infty = 0.4$, $\alpha = 0^o$ and $Re_c = 5.0 \times 10^6$. The computed loads for the steady–state computation did not show variation in time. A time–accurate computation was then carried out for a long time, $T \approx 40$ nondimensional time units. The computed loads for the RC(6) – 08 6^o slat airfoil, for the leading–edge flap alone, and for the wing alone are shown in Fig. 2. It is seen that at the plot scale the computed drag has a periodic variation in time. Closer inspection of the computed lift (see Fig. 3) shows that the lift coefficient also shows an almost sinusoidal variation in time. It was found that the largest unsteadiness in the computed solution is in the leading edge region.

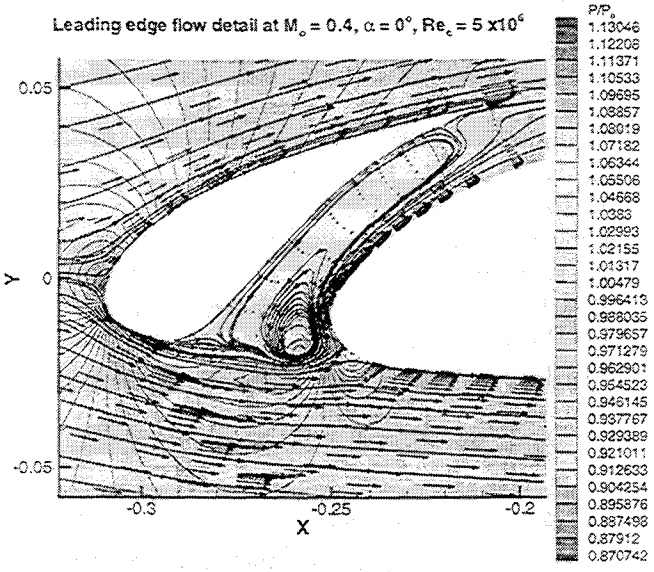

Fig. 4 Snapshot of the computed flowfield at the leading edge of the RC(6) – 08/106 airfoil. $M_\infty = 0.4, \alpha = 0.0^o, Re_c = 5 \times 10^6$ (fully turbulent).

The computed leading–edge flowfield structure is shown with the instantaneous velocity vectors and and pressure field in Fig. 4. The instantaneous streamlines clearly show the formation of a vortex in the slat region. The self excited unsteady flow behavior is generated by the continuous shedding of vortices through the slat region. These vortices are subsequently convection over the airfoil surface and cause load variations. These vortices are formed only at small angles of incidence. Computed solutions for angles of incidence $\alpha > 3^o$ have not captured similar unsteady flow behavior and predicted a mild quasi–steady flow separation in the slat region which did not result into vortex shedding.

3.2 Dynamic Stall of slatted airfoils

Computations are carried out for the oscillatory motion $\alpha(t) = 10^o + 10^o \sin(\omega t)$ with nondimensional reduced frequency $k = 0.05$. The computed flowfields at a low incidence, $\alpha = 0.5^o$, and high incidence, $\alpha = 18.5^o$, during the upstroke are shown in Fig. 5.

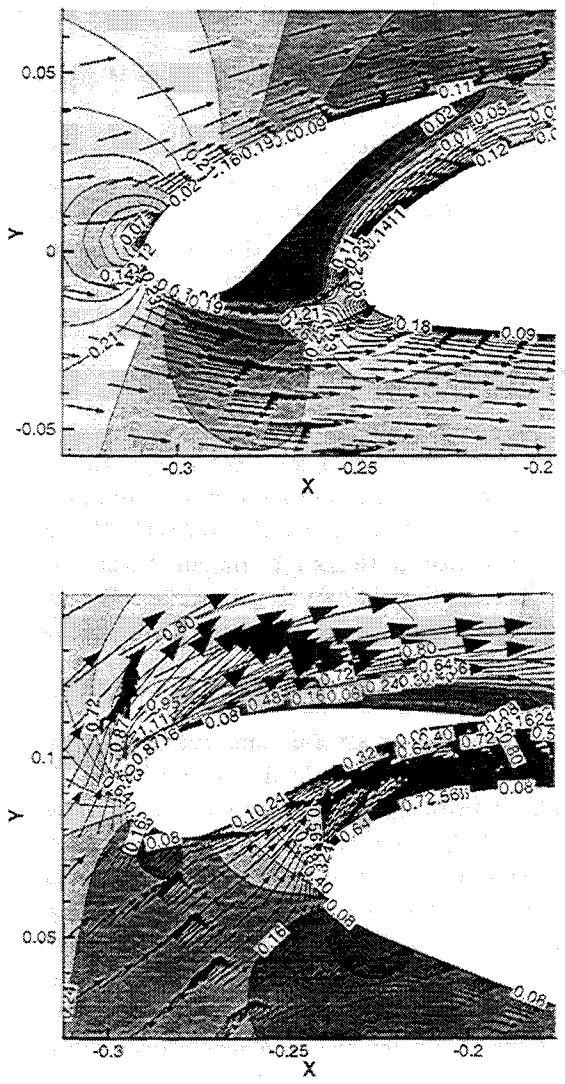

Fig. 5 Snapshot of the computed flowfield at the leading edge of the RC(6) – 08/106 airfoil at $\alpha = 0.5^o$ and $\alpha = 18.5^o$ for oscillatory motion $\alpha(t) = 10^o + 10^o \sin(\omega t)$; $M_\infty = 0.4, \alpha = 0.0^o, Re_c = 5 \times 10^6$ (fully turbulent).

The flowfield is shown with the velocity vectors (both drawn at the same scale) and the Mach number contours. At low incidence the computed flowfield shows a recirculation flow region at the leading edge which

resembles the flow computed for $\alpha = 0^o$ fixed angle of incidence. At high incidence, $\alpha = 18.5^o$, the supersonic flow region which form at the leading edge terminates into a shock wave which causes separation of the flow over the flap.

The computations for the baseline RC(6)–08 airfoil, airfoil with the 6^o slat and that with the 10^o slat are compared in Fig. 6 and 7 for $\alpha(t) = 10^o + 10^o sin(\omega t)$ at a freestream Mach number of $M_\infty = 0.4$. The steady flow experimental [13] lift, drag, and pitching moment coefficients are also shown in these figures. The computations clearly show that the results follow the steady flow values until the airfoil is pitched past the static stall angle. The baseline airfoil experiences significant dynamic stall and hence, the force and moment loops show a large hysteresis effect. Load oscillations during the downstroke are attributed to the unsteady reattachment of the flow for part of the time and over part of the airfoil. The computed flowfields show that dynamic stall initiates because of separated flow at the leading edge. Flow separation is triggered by a shock forming at the leading edge during the upstroke. This shock forms at approximately 10^o angle of incidence, and as it becomes stronger with increasing incidence, causes separation of the leading edge boundary layer.

In comparison to the baseline airfoil, the loops for the 6^o slat case show much smaller hysteresis loops and no oscillations. A significant result is the largely improved drag values and even more significant is the almost flat pitching moment distribution. This indeed is the benefit of using the slatted airfoil for dynamic stall control. The experimental data for this airfoil [3] oscillated as $\alpha(t) = 10^o + 10^o sin(\omega t)$ also showed that the airfoil experienced a softer dynamic stall. The above computational results serve to emphasize the degree of control that can be achieved using a slatted airfoil.

The same experiments [3] for the 10^o slat case showed that the flow once again experienced mild dynamic stall, however, attributable to the formation of a shock in the slat passage and over the airfoil subsequently. The present computations for the 10^o slat case (Fig. 7) show a slightly larger hysteresis in the lift loop compared to the 6^o slat case, but a largely increased drag loop. For this case dynamic stall effects are stronger because the slat becomes ineffective after the formation of a shock in the slat region at approximately sixteen degrees angle of incidence during the upstroke. The pitching moment is also larger than the 6^o case, leading to the result that the 10^o slat may not be as effective in achieving dynamic stall control.

3.3 Pulsating Jet Flow Control

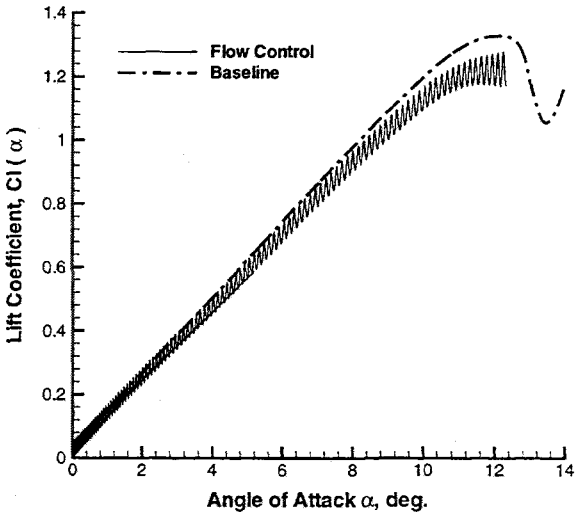

Fig. 8 Comparison of the computed lift coefficient with and without flow control.

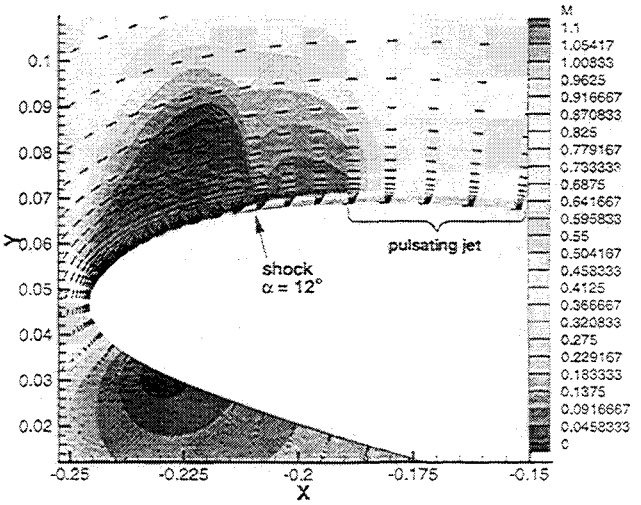

Fig. 9 Snapshot of the computed flowfield with leading edge pulsating jet flow control for the baseline airfoil at $\alpha = 12^o$; oscillatory motion $\alpha(t) = 10^o + 10^o \sin(\omega t)$; $M_\infty = 0.4, \alpha = 0.0^o, Re_c = 5 \times 10^6$ (fully turbulent).

It has been demonstrated in the experiments [11] that the important parameters for airfoil flow control with pulsating jets are the reduced excitation frequency, $F^+ = f_J c/U_\infty$, where c is the airfoil chord and f_J is the jet pulsation frequency, and the oscillatory blowing momentum coefficient, $C_\mu = < J > /cq$, where $q = 0.5\rho U_\infty^2$, $< J >$ is the oscillatory momentum, $< J >= \rho V_J^2 H_J$, where H_J is the jet slot width, and V_J is the jet velocity oscillation amplitude. The

jet pulsation frequency in these simulations was fixed, $F^+ = 0.6$, and the momentum coefficient varied as $2.5\% < C_\mu < 5.0\%$.

Simulations of active flow control with a pulsating jet applied at the leading edge region of the baseline RC(06)–08 airfoil were carried out. A jet slot width, H_J, of the same order of magnitude as the width of leading–edge slat of the slatted airfoils, presented in the previous section, was used in the numerical simulations. In order to enhance the flow control effectiveness, high values of blowing coefficient C_μ were prescribed. The jet output velocity reached values up to 75% the free stream speed in order to approximate the high speed flow observed in the slat region for high incidences.

For the wide range of jet output levels considered, it was not possible to obtain effective flow control at the leading edge of the baseline airfoil. It was found, that at approximately 10^o angle of incidence during the upstroke a shock wave developed at the leading edge, similar to the case without flow control. This shock become stronger as the angle of incidence increased. Flow control delayed shock induced flow separation by approximately one degree, however, the separated at approximately $\alpha = 12^o$. Beyond this angle of incidence the pulsating flow control becomes ineffective and the computed loads do not show any improvement compared to the loads obtained computation without flow control. A comparison of the computed lift during the upstroke is shown in Fig. 8. The computed flowfield at $\alpha = 12^o$ where the flow separates at the leading edge is shown in Fig. 9.

Flow controls with pulsating zero net mass flux jets were found effective for the control of dynamic stall occurring at smaller oscillation amplitudes and lower free stream speeds. Several load hysteresis loops obtained from controlled compressible flow dynamic stall over a NACA–0015 airfoil at $M_\infty = 0.3$ oscillating as $\alpha(t) = 13^o + 5^o sin(\omega t), k = 0.05$ are shown in Fig. 10. The computed load hysteresis loop for control with a pulsating jet located at $x_J/c = s_J = 0.1$ and actuation parameters $F^+ = .31$ and $C_\mu = 2.5\%$ is compared in Fig. 10 with the high Reynolds number measurements of Ref. [14]. The high pulsation level of the jet ($C_\mu = 2.5\%$) reduces the dynamic stall hysteresis effects effectively but causes a significant oscillation of the loads at the jet pulsation frequency. The computed load hysteresis loop for control of compressible flow dynamic stall obtained by a pulsating jet located at $s_J = 0.7$ with $F^+ = .31$ and $C_\mu = 2.5\%$ is shown in the same figure. The high output of the jet ($C_\mu = 2.5\%$) reduces the dynamic stall hysteresis effects effectively and for the location $s_J = 0.7$ causes a small oscillation of the loads at the jet pulsation frequency. The reductions of the maximum excursions of the drag, $Cd(\alpha)$, and pitching moment, $Cm(\alpha)$, coefficients are significant.

4 Summary

Numerical simulations of passive and active flow controls were carried out. It was found that at low angles of incidence leading–edge slats can generate unsteady flow. The leading–edge slats were proven as an effective flow control mechanism of dynamic stall generated by large amplitude oscillatory motion and high speed flow with significant compressibility effects. Pulsating jet flow control was not able to eliminate shock induced leading edge flow separation and was ineffective in suppressing dynamic stall unsed these conditions. However, application of pulsating jet flow control to oscillating airfoils at lower free stream speed was found quite effective.

References

[1] Bangalore, A. and Sankar, N. L., "Forward–Flight Analysis of Slatted Rotors Using Navier–Stokes Methods," *Journal of Aircraft,* Vol. 34, No. 1, 1997, pp. 80–86.

[2] Chandrasekhara, M. S., Wilder, M. C., and Carr, L. W., "Compressible Dynamic Stall Control Using a Shape Adaptive Airfoil," AIAA 99-0650, 1999.

[3] Chandrasekhara, M. S., Wilder, M. C., and Carr, L. W., "Compressible Dynamic Stall Control: A Comparison of Different Approaches," AIAA 99-3122, 1999.

[4] Ekaterinaris, J. A. and Menter, F. R., "Computation of Oscillating Airfoil Flows with One– and Two–Equation Turbulence Models," *AIAA Journal,* Vol. 32, No. 12, 1994, 2359–2365.

[5] Ekaterinaris, J. A., "Numerical Investigation of Dynamic Stall of an Oscillating Wing," *AIAA Journal,* Vol. 33, No. 10, 1995, pp. 1803–1808.

[6] Ekaterinaris, J. A., Chandrasekhara, M. S., and Platzer, M. F., "Analysis of Low Reynolds Number Airfoils," *Journal of Aircraft,* Vol. 32, No. 3, May–Jun. 1995, pp. 625–630.

[7] Ekaterinaris, J. A. and Platzer, M. F., "Computational Prediction of Dynamic Stall," *Progress in Aerospace Sciences,* Vol. 33, No. 11–12, 1997, pp. 759–846.

[8] Ekaterinaris, J. A., Sorensen, N. N., and Rasmussen, F., "Numerical Investigation of Airfoil Dynamic Stall in Simultaneous Oscillatory and Translational Motion," *ASME Journal of Solar Energy Engineering,* Vol. 120, 1998, pp. 75–83.

[9] Ekaterinaris, J. A., "Numerical Investigation of Dynamic Stall Active Control for Incompressible and Compressible Flows," AIAA Paper 2000–4333, 2000.

[10] Greenblatt, D., Nishiri, B., Dabari, A., and Wygnanski, I., "Some Factors Affecting Stall Control with Particular Emphasis on Dynamic Stall," AIAA 99-3504, 1999.

[11] Greenblatt, D. and Wygnanski, I., "Parameters Affecting Dynamic Stall Control by Oscillatory Excitation," AIAA 99-3121, 1999.

[12] McAlister, K.W., Pucci, S. L., McCroskey, W. J., and Carr, L. W., "An Experimental Study of Dynamic Stall on Advanced Airfoil Sections, Volume 2: Pressure and Force Data," NASA–TM 84254, Sept. 1982.

[13] Noonan, K. W., Allison, D. O. , and Stanaway, S., "Investigation of a Slatted Rotorcraft Airfoil at Mach Numbers from 0.20 to 0.88 at Full Scale Reynolds Numbers," American Helicopter Society, Aerodynamics Specialist Conference, San Francisco, CA Jan. 1994.

[14] Piziali, R. A., "2–D and 3–D Oscillating Wing Aerodynamics for a Range of Angles of Attack Including Stall," NASA–TM 4632, 1994.

[15] Roe, P. L., Approximate Riemann Solvers, Parameter Vectors, and Difference Schemes, *Journal of Computational Physics,* Vol 43, No. 2, 1981, pp. 357–372.

[16] Seifert, A. and Pack, L. G., "Oscillatory Control of Separation at High Reynolds Numbers," *AIAA Journal,* Vol. 37, No. 9, 1999, pp. 1062–1079.

[17] Spalart P. R., and Allmaras, S. R., "A One-Equation Turbulence Model for Aerodynamic Flows," AIAA Paper 92–0439, 1992.

[18] Tuncer, I. and Sankar, N. L., "Unsteady Aerodynamic Characteristics of a Dual–Element Airfoil," *Journal of Aircraft,* Vol. 31, No. 3, 1994, pp. 531–537.

[19] Weaver, D., McAllister, K. W., and Tso, J., "Suppression of Dynamic Stall by Steady and Pulsed Upper-Surface Blowing," AIAA 98-2413, 1998.

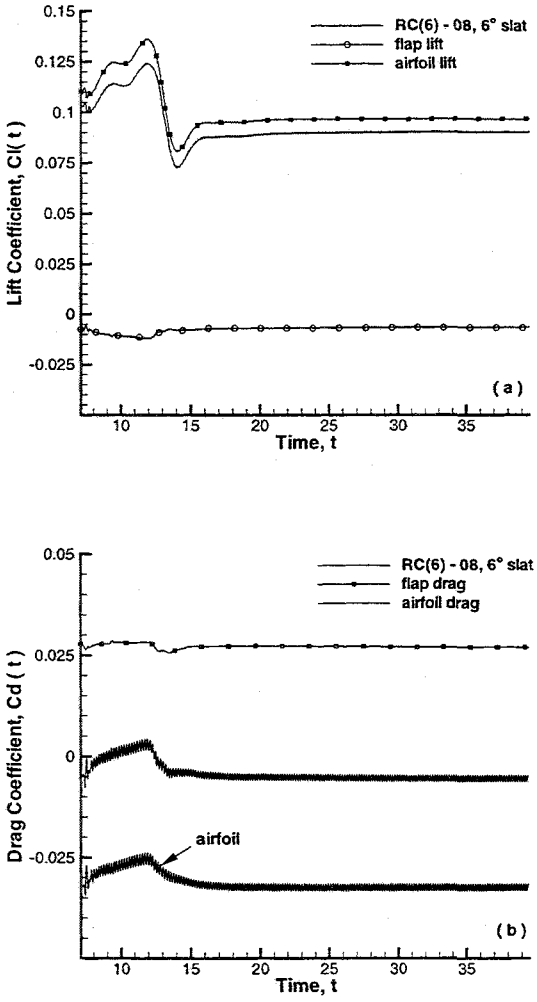

Fig. 2 Computed loads for RC(6) − 08, 6° slat airfoil; $M_\infty = 0.4, \alpha = 0^o, Re_c = 5 \times 10^6$ (fully turbulent).

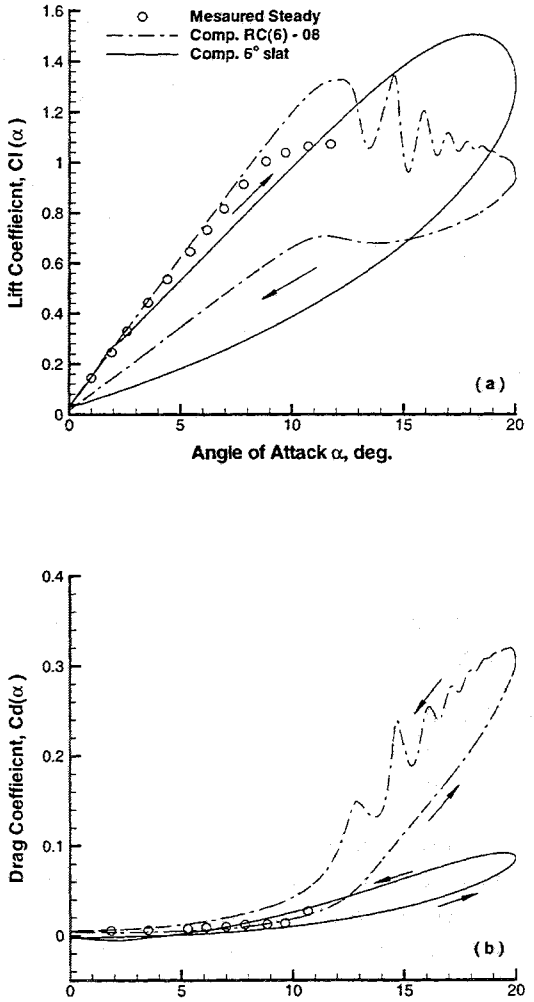

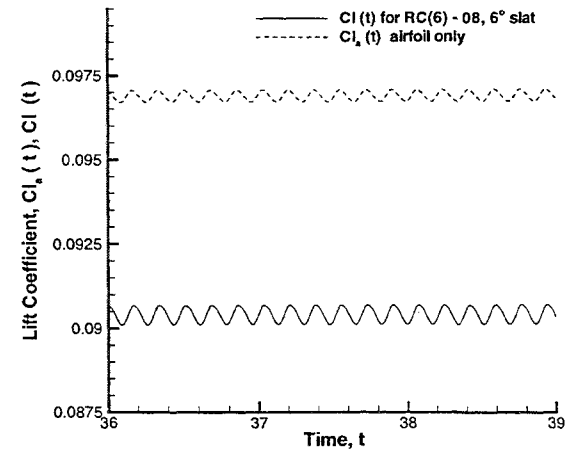

Fig. 3 Time variation of the computed lift for RC(6) − 08, 6° slat airfoil; $M_\infty = 0.4, \alpha = 0^o, Re_c = 5 \times 10^6$ (fully turbulent).

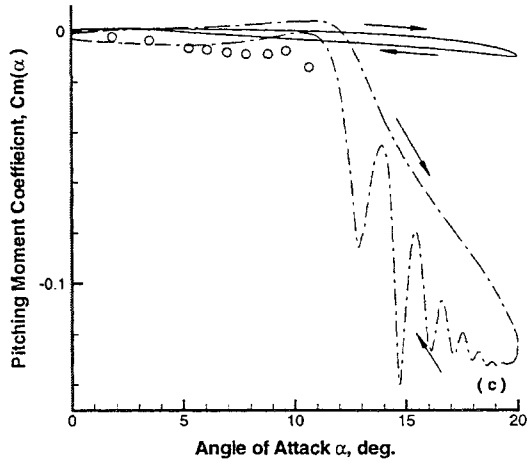

Fig. 6 Comparison of the computed and mesured loads for the baseline and 6° slat airfoils. $M_\infty = 0.4, \alpha(t) = 13^o + 5^o sin(\omega_a t), k = 0.05, Re_c = 5.0 \times 10^6$ (fully turbulent),

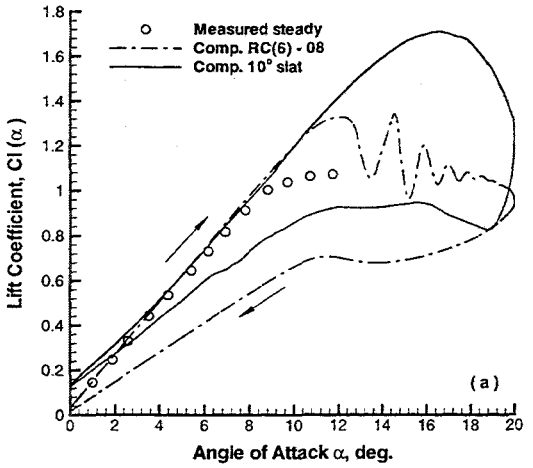

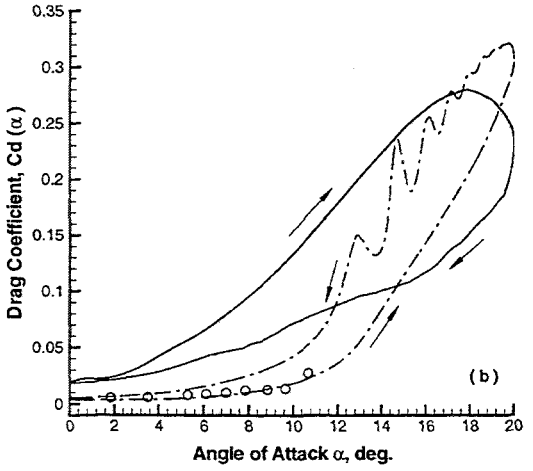

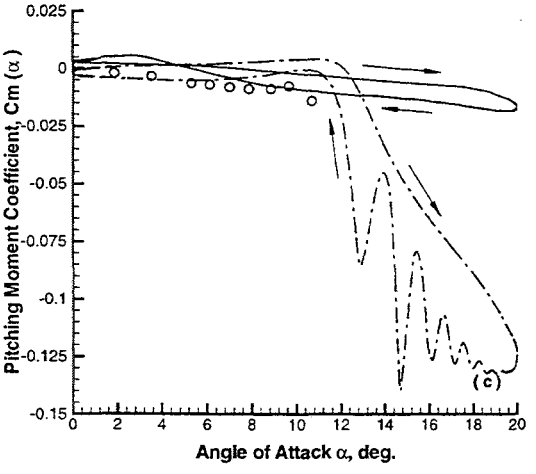

Fig. 7 Comparison of the computed and mesured loads for the baseline and 10^o slat airfoils. $M_\infty = 0.4, \alpha(t) = 13^o + 5^o sin(\omega_a t), k = 0.05, Re_c = 5.0 \times 10^6$ (fully turbulent).

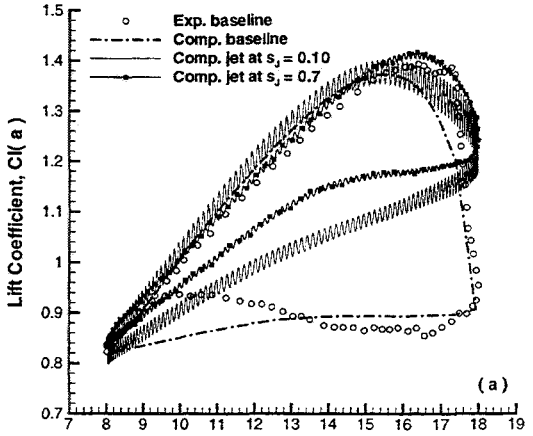

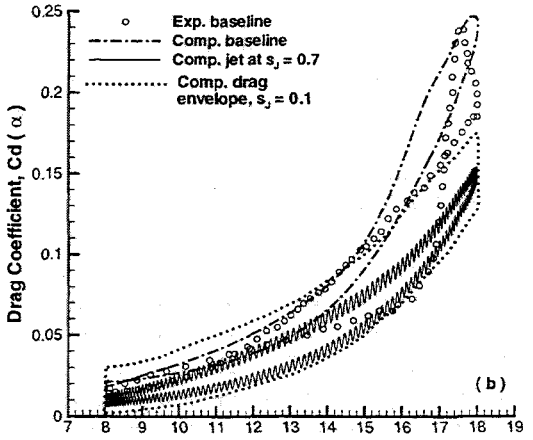

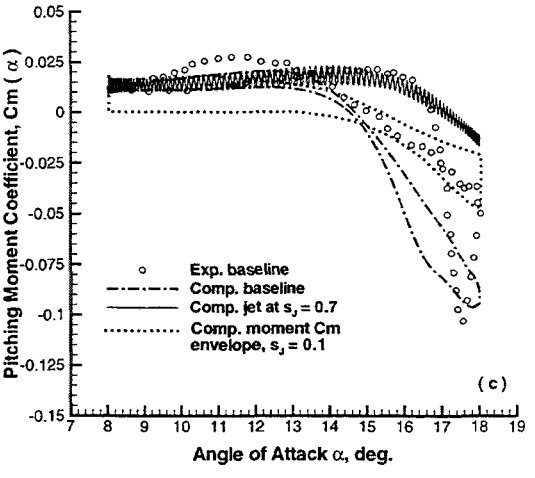

Fig. 10 Comparison of the computed and mesured loads. Computatin at $Re_c = 5.0 \times 10^6$ (fully turbulent), $\alpha(t) = 13^o + 5^o sin(\omega_a t), k_a = 0.05$, $F_J^+ = 0.31$, jet pulsation level, $C_\mu = 2.5\%$.